Materials Advances

ROYAL SOCIETY OF CHEMISTRY

PAPER

View Article Online
View Journal

Cite this: DOI: 10.1039/d6ma00366d

Photodimerization induced photomechanical behaviour in alkyldiammonium salts of *trans*-dichlorocinnamates: exploration of [2+2] reactions in as-synthesized salts, single crystals and organogels

Shaheen Sultana, Debasis Pal and Kumar Biradha *

The development of light-responsive molecular crystals that convert light into mechanical energy is a burgeoning field with applications ranging from remote actuation to flexible electronics. This study explores the [2+2] photodimerization and subsequent photomechanical behaviour of a series of organic salts synthesized from alkyldiamines (H_2N-$(CH_2)_n$-NH_2, n = 2–4) B_n and *trans*-2,4/3,4-dichlorocinnamic acid (A_{m4}, m = 2–3). By employing chloro-substitution to direct crystal packing into photoreactive β-type structures, we investigated these reactions across three distinct states: as-synthesized salts, single crystals, and supramolecular organogels. The experimental results demonstrate that salts containing ethylenediamine ($B_2(A_{24})_2$) and propylenediamine ($B_3(A_{24})_2$) are photoactive across all states, while butylenediamine ($B_4(A_{24})_2$ & $B_3(A_{24})_2$) derivatives remain photoinactive. Notably, the [2+2] reaction in single crystals of $B_2(A_{24})_2$ and $B_3(A_{24})_2$ induced dramatic photomechanical effects, including macroscopic bending, surface peeling, and the formation of surface cracks. The successful formation of cyclobutane dimers was confirmed *via* ^{1}H-NMR, MALDI-ToF mass spectra, and single-crystal X-ray diffraction. Furthermore, we report a rare instance of organogels derived from these simple organic salts undergoing [2+2] photodimerization while exhibiting significant electrical conductivity (5.2×10^{-3} S cm^{-1}). Additionally, certain salt compositions demonstrated high efficiency for iodine absorption. This work highlights the versatility of organic diammonium salts as multifunctional materials for optomechanics, sensing, and conducting soft materials.

Received 15th March 2026,
Accepted 11th May 2026

DOI: 10.1039/d6ma00366d

rsc.li/materials-advances

Introduction

The transformation of light energy into mechanical energy in molecular crystals is a rapidly advancing research area, harnessing solid-state reactivity to produce rapid, efficient movements in remote actuation, artificial muscles, microdevices, and flexible electronics.[1–5] Light-responsive crystalline materials exhibit dynamic mechanical responses, such as fracturing,[6] twisting,[7] jumping,[8,9] or bending,[10,11] that often arise from rapid structural changes and internal strain accumulation within the crystal lattice. Photomechanical deformations are primarily attributed to photochemical reactions or photoisomerization occurring within crystals. Classic examples include [2+2] photodimerization[12] of olefins and [4+4] photodimerization of anthracenes.[13–15] Some organic solids, metal complexes and coordination polymers exhibit photomechanical motions so intense that they lead to explosions or shattering, akin to popcorn popping on a hot plate.[16–20] Vittal and co-workers have extensively studied the photomechanical effect associated with [2+2] photodimerization of 4-styrylpyridine[21,22] and 1,2-di(4-pyridyl)ethylene.[23] Bardeen *et al.* demonstrated photomechanical deformation in crystalline materials *via* the [4+4] photodimerization of 9-tert-butylanthroate (9-TBAE) nanorods.[24] More recently, Biradha and co-workers reported [2+2] photopolymerization in single crystals of flexible dienes, which induced significant bending of the crystals.[25] In addition to crystalline solids, soft materials such as polymers,[26] hydrogels,[27] and liquid crystals also exhibit photomechanical properties.[28] Despite the remaining fundamental and practical hurdles, emerging uses of soft robotics, optoelectronic materials, and optical switches demonstrate the significant potential for photomechanical crystals in upcoming technologies. However, studies of photomechanical properties in crystals offer valuable insights into their internal response mechanisms, given the availability of their precise structural information.

Department of Chemistry, Indian Institute of Technology Kharagpur, Kharagpur 721302, West Bengal, India. E-mail: kbiradha@chem.iitkgp.ac.in

Several crystalline organic solids are being deliberately designed to achieve topochemical [2+2] cycloaddition reactions by precisely controlling intermolecular forces and molecular packing arrangements.[29] Carboxylate salts of organic amines are extensively employed for screening functional organic crystalline materials, including host–guest crystals,[30] crystalline-state photoreactions,[31,32] topochemical polymerizations,[33] and organogelators.[34] Organic salts offer key advantages given their simple preparation and the creation of materials containing strong charge-assisted hydrogen bonds. A notable example of a carboxylate salt of an amine was reported by Ramamurthy and coworkers, where light triggers large molecular motions in the crystals. In this example, irradiation of a double salt formed between 1,2-*trans*-diaminocyclohexane and *trans*-2,4-dichlorocinnamic acid results in mirror symmetric β-truxinic acid *via* pedal motion of the olefins in the solids.[35] Furthermore, salts of cinnamic acid with a series of alkyl diamines (H_2N-$(CH_2)_n$-NH_2, n = 2–6) were also shown to undergo [2+2] reaction upon irradiation.[36,37] Furthermore, crystalline organic salts have gained interest for applications in gas capture,[38] catalysis,[39] conductivity[40] and molecular separations.[41] Recently, Cooper *et al.* reported isoreticular ammonium halide salts as potential alternatives to porous metal–organic frameworks (MOFs), showing promising high level iodine capture efficiency at 70 °C.[42] On the other hand, primary ammonium monocarboxylates were shown as low-molecular-weight gelators (LMWGs) *via* the formation of one-/two-dimensional hydrogen-bond networks.[43] In these soft materials, one-dimensional anisotropic interactions restrict lateral fiber growth, producing highly branched one-dimensional fibers that entangle to form a three-dimensional network, thereby immobilizing the solvent.[44] In addition, gels provide a versatile platform for the promotion of many organic reactions involving covalent bond formations.[45] We have shown earlier that [2+2] dimerization and polymerization reactions progress smoothly both in organogels (OGs) and metal–organic gels (MOGs).[46–49] However, a supramolecular organogel derived from simple organic salts capable of [2+2] photodimerization hasn't been reported to date.

Herein, we have exploited the strategy of salt formation between alkyl diamines (H_2N-$(CH_2)_n$-NH_2, n = 2–4) B_n and two monocarboxylic acids, namely *trans*-2,4/3,4-dichlorocinnamic acid (A_{m4}, m =2–3), to study the photodimerization reactions in the as-synthesized salts, single crystals and organogels (Scheme 1). The chloro-substitution on the aromatic ring of cinnamic acids is anticipated to direct the packing to β-type structures, which promotes [2+2] reactions (Scheme S1).[50–52] Among the six possible combinations, crystals suitable for single crystal diffraction analysis were obtained for $B_2(A_{24})_2$, $B_3(A_{24})_2$, $B_4(A_{24})_2$ and $B_4(A_{34})_2$. All the as-synthesized salts of B_2 and B_3 were found to exhibit [2+2] reaction upon irradiation, whereas B4 salts are photoinactive. Similar reactivity is also observed in their respective single crystals. Interestingly, the [2+2] reaction in the crystals of $B_2(A_{24})_2$ and $B_3(A_{24})_2$ accompanied bending, fragmentation and the development of cracks on the crystal surface. ^{1}H-NMR, Matrix-Assisted Laser Desorption Ionization analysis (MALDI-ToF) and single crystal structures

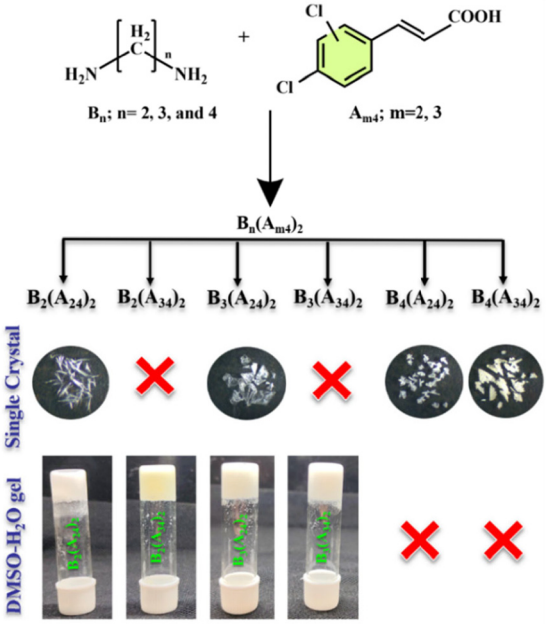

Scheme 1 Representation of the molecular structures and corresponding alkyldiammonium salts studied herein, along with photographs of their single crystals and organogels. The materials that failed to produce good quality single crystals or gels are represented with a cross.

confirmed the formation of photo-dimers. Among the six possible combinations, four combinations, namely $B_2(A_{24})_2$, $B_2(A_{34})_2$, $B_3(A_{24})_2$ and $B_3(A_{34})_2$, were able to form organogels both in protic and aprotic solvents, owing to their extensive hydrogen-bonded network and good solubility. The organogels were also found to undergo [2+2] photodimerization upon irradiation. Furthermore, the gels were found to show significant electrical conductivity (5.2×10^{-3} S cm^{-1}) as well. The as-synthesised B_3 and B_4 salts of A_{m4} exhibited excellent ability for iodine absorption.

Results and discussion

The *trans*-2,4/3,4-dichlorocinnamic acids (A_{24}/A_{34}) were synthesised using Knoevenagel condensation reaction between 2,4/3,4-dichloro benzaldehyde and malonic acid.[35] The ammonium salts were synthesized by reacting two equivalents of alkyl diamine (B_{2-4}) with one equivalent of cinnamic acid (A_{24} or A_{34}) in methanol at ambient temperature, yielding the salts in nearly quantitative amounts (Fig. S1, SI). Crystals suitable for single-crystal X-ray diffraction (SCXRD) analysis were obtained *via* slow evaporation from suitable solvents (Scheme 1 and Table S1, SI) in 3-4 days. Despite our best efforts, diffraction-quality single crystals of $B_2(A_{34})_2$ and $B_3(A_{34})_2$ could not be obtained. The single crystals of $B_2(A_{24})_2$ & $B_2(A_{34})_2$ are found to be photoreactive upon exposure to 365 nm UV light. Notably, after a few hours of irradiation, the $B_2(A_{24})_2$ crystals exhibited visible bending, while the $B_3(A_{24})_2$ crystals displayed visible cracks and surface peeling, known as photomechanical behaviour.

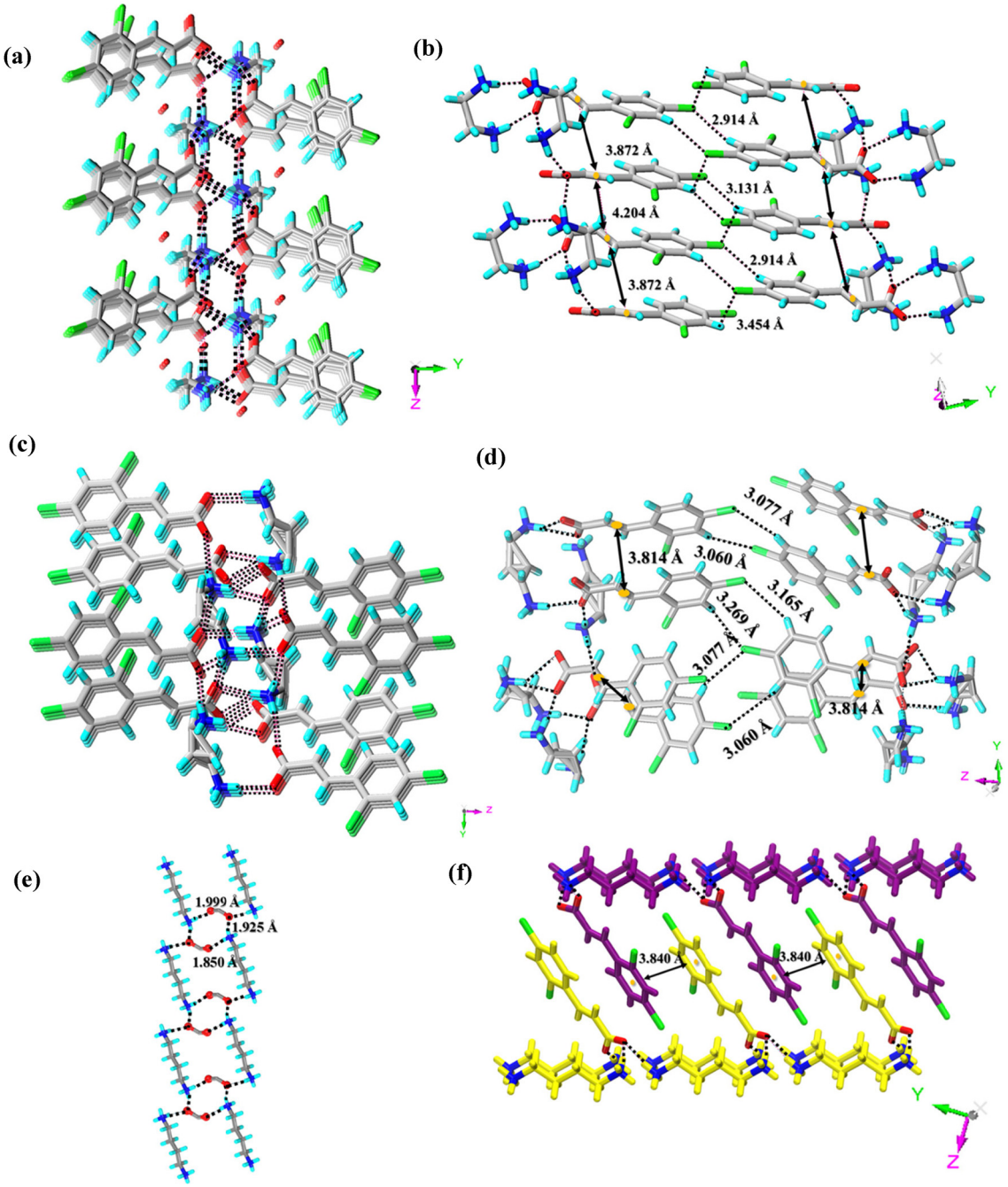

Fig. 1 Illustrations of the crystal structures of $B_2(A_{24})_2$, $B_3(A_{24})_2$ and $B_4(A_{24})_2$: the bilayer type of hydrogen bonding in (a) $B_2(A_{24})_2$ and (c) $B_3(A_{24})_2$; the alignment of double bonds and Cl···Cl interactions in (b) $B_2(A_{24})_2$ and (d) $B_3(A_{24})_2$; (e) the hydrogen-bonded layer and (f) interdigitation of cinnamate anions in the packing of the layers in $B_4(A_{24})_2$.

SCXRD analysis revealed that $B_2(A_{24})_2$ crystallises in the monoclinic $P2_1/c$ space group, whereas $B_3(A_{24})_2$ crystallises in the orthorhombic *Pbca* space group. The asymmetric units of both the salts contain two units of 2,4-dichlorocinnamate anions and one unit of the corresponding diammonium cation (disordered site occupancy in the case of propane diamine). $B_2(A_{24})_2$ contains two additional water molecules in its asymmetric unit as well. Carboxylate anions are involved in charge-assisted N–H···O hydrogen bonding with the alkyl diammonium cations (Fig. 1a and c). Two carboxylates of $B_2(A_{24})_2$ form four N–H···O hydrogen bonds with the ethylene-diammonium cation (N···O: 2.765(6) Å–3.203(7) Å; < N–H···O: 128°–172°). In contrast, in $B_3(A_{24})_2$, the carboxylates form a total of seven N–H···O hydrogen bonds with the propanediammonium cation (N···O: 2.711(7) Å–3.121(7) Å; < N–H···O: 102°–166°, Table S2, SI). Such type of hydrogen-bonding generates a two-dimensional layer with dangling dichloro-aromatic groups on one side of the layer.

The layers pack to form a bilayer structure of alternating hydrophilic and hydrophobic layers (Fig. S3). The hydrophobic layers interact with each other by abundant C–H···Cl (Table S2, SI) and type II Cl···Cl (Table S3, SI) interactions.[53] The water molecules in $B_2(A_{24})_2$ form two O–H···O hydrogen bonds with a carboxylate anion and one O–H···O hydrogen bond among themselves (Table S2, SI). In both the structures, the olefinic double bonds are found to have reactive alignment with distances of 3.872 Å and 4.204 Å in $B_2(A_{24})_2$ and 3.814 Å in $B_3(A_{24})_2$ (Fig. 1b and d). The powder X-ray diffraction pattern (PXRD) of the as-synthesised $B_2(A_{24})_2$ and $B_3(A_{24})_2$ salts agrees well with the simulated pattern of their single crystals (Fig. S2, SI).

The crystal structure analyses of $B_4(A_{24})_2$ and $B_4(A_{34})_2$ revealed that both are isostructural and crystallise in the $P\bar{1}$ space group. The asymmetric units contain one unit of corresponding dichlorocinnamate and half a unit of 1,4-diammonium butane, which displays all-anti conformation in both cases with dihedral angles of 178°–178.9°. The hydrogen bonding between carboxylates and alkyl diammonium cations (N···O: 2.770(3) Å–3.405(3) Å; < N–H···O: 155°–174° for $B_4(A_{24})_2$ and N···O: 2.752(4) Å–3.285(5) Å; <N–H···O: 136°–168° for $B_4(A_{34})_2$) leads to the formation of a hydrogen bonded layer (Fig. 1e) with dichlorocinnamate groups projecting from both sides of the layers. The layers pack such that there is interdigitation of the cinnamate groups, which was supported by π···π interactions between the cinnamates with head-to-tail stacks and C–H···Cl and Cl···Cl interactions (Fig. 1f). The head-to-tail stacking of the cinnamates places the C=C bonds beyond the [2+2] reactive distance.

The gelation experiments were conducted with all six as-synthesized materials in three different solvent systems. Four of the six materials were found to form gels, while $B_4(A_{24})_2$ and $B_4(A_{34})_2$ (Table S4, SI) did not. The three successful solvent systems for gelation are found to be DMSO, DMSO/water and nitrobenzene. While $B_2(A_{24})_2$ demonstrated robust gelation across all three solvent systems, $B_2(A_{34})_2$ formed stable gels only in DMSO and DMSO/water. Furthermore, its nitrobenzene gel was significantly weaker, failing to maintain its own weight after a few minutes. $B_3(A_{24})_2$ and $B_3(A_{34})_2$ only form stable gels in DMSO/water. The gelation process was confirmed from an inverted vial test and they exhibit a critical gelation concentration (CGC) of 10–20 mg ml^{-1}. The organogels display thermo-reversible nature. The oscillatory shear experiments, including amplitude and frequency sweeps, were conducted at room temperature to investigate the viscoelastic properties of these gels.

First, seven organogel samples were sheared in strain sweep experiments with a constant frequency of 10 rad s^{-1} (amplitude sweep experiment) to determine the linear viscoelastic range or limiting strain (σ_y) for performing the frequency sweep experiments (Fig. 2a, c and Fig. S4, SI). Frequency sweep experiments were carried out under 0.1% strain, as suggested by amplitude sweep experiments. In all cases, the values of the storage or elastic modulus (G') were larger than those of the loss or viscous modulus (G'') and they were frequency invariant over the entire range of angular frequency, ω (Fig. 2b, d and Fig. S4, SI); this revealed typical viscoelastic behaviour. The aqueous-DMSO gel of $B_2(A_{24})_2$ was found to be the strongest (G'–G'' ≈ 750 kPa) of all the gels studied herein (Table 1). The high-resolution transmission electron microscopic (HRTEM) images of the aqueous-DMSO gel mostly showed a popsicle stick-like morphology for $B_2(A_{24})_2$, $B_2(A_{34})_2$ and $B_3(A_{24})_2$, whereas both the FESEM and HRTEM images displayed a plate-kind of morphology for the $B_3(A_{34})_2$ gel (Fig. 2e–h and Fig. S5, SI). The PXRD patterns of the aqueous-DMSO xerogels were compared with the single crystals and as-synthesised gelator salts. As shown in Fig. S6, the diffraction peak matches well in all cases except for $B_2(A_{34})_2$, indicating that the xerogel typically possesses the same phase as the as-synthesized material.

The photochemical reactions were carried out on all crystals, as-synthesized materials, and freshly prepared aqueous-DMSO

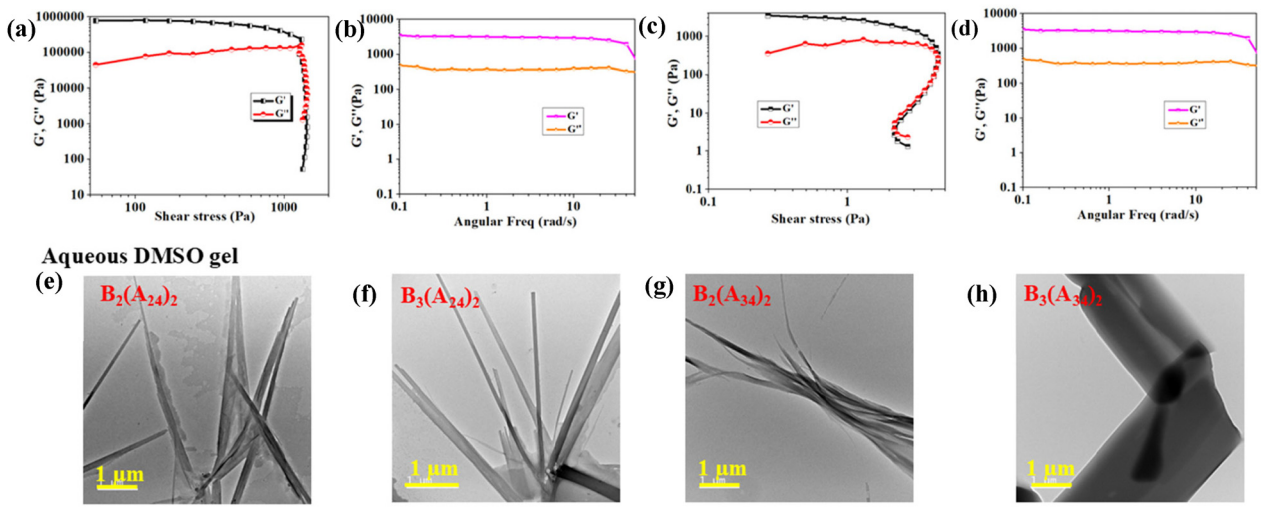

Fig. 2 Illustrations of the rheological measurements of the aqueous-DMSO gels of $B_2(A_{24})_2$ (strongest) and $B_3(A_{34})_2$ (weakest): (a) and (c) amplitude sweep, (b) and (d) frequency sweep; (e)–(h) HRTEM images displaying different morphologies.

Table 1 Yield stress (σ_y), rigidity (G'–G'') and morphology of the various organogels

Gel	Yield stress (σ_y Pa)	G'–G'' (Pa)	Morphology
$B_2(A_{24})_2$ (aqueous-DMSO)	1300	754 280	Popsicle stick
$B_2(A_{24})_2$ (DMSO)	160	53 710	Popsicle stick
$B_2(A_{24})_2$ (Ph-NO_2)	217	69 186	Oval plate shape
$B_2(A_{34})_2$ (aqueous-DMSO)	47	22 877	Popsicle stick
$B_2(A_{34})_2$ (DMSO)	46	6910	Scattered popsicle stick
$B_3(A_{24})_2$ (aqueous-DMSO)	61	21 606	Popsicle stick
$B_3(A_{34})_2$ (aqueous-DMSO)	5	2952	Rectangular plate shaped

gels by irradiation at 365 nm in a UV chamber. As suggested by the crystal structures, two of the samples underwent near-quantitative photochemical [2+2] dimerization within different time frames, as confirmed by ^{1}H NMR and MALDI-ToF analyses. The ^{1}H NMR spectra show the emergence of head-to-head (HH) cyclobutane peaks at δ values of 4.58 and 3.91 ppm for $B_2(A_{24})_2$ and $B_3(A_{24})_2$ (Fig. S7 and S10, SI), indicating the formation of a HH-*rctt*-2,4cpcb dimer (cpcb = dichlorophenyl cyclobutane).[32,47] The % yield of photodimerization after 24 h of UV irradiation is given in Table 2. Moreover, when the as-synthesised $B_2(A_{34})_2$ and $B_3(A_{34})_2$ salts were irradiated, they also exhibited cyclobutane peaks at δ values of 4.10 and 3.59 ppm, corresponding to HH-*rctt*-3,4cpcb (Fig. S9 and S11, SI), indicating successful [2+2] photodimerization. The ^{1}H NMR spectra of the irradiated gels suggest that all B_2 and B_3 salts underwent [2+2] photodimerization in ~29–72% yields within 24 h (Fig. S7–S11, SI). The appearance of a doublet of doublets at nearly the same chemical shift as the crystals confirms head-to-head dimer formation. However, the reactions in the gel state proceeded more slowly compared to the as-synthesized and single crystals. Contrary to a few instances where gel-to-gel or gel-to-sol transformation[46–49] leads to quantitative photocycloaddition, the organogels in this study cannot withstand the structural changes during photoreaction due to their weak mechanical rigidity. This results in a loss of 'topochemical control' leading to poorer yields (~30% conversion) compared to the crystalline salts. The formation of the dimer was further confirmed by the *m*/*z* peak at 431.92 in MALDI-ToF analysis (Fig. S14, SI).

Interestingly, the crystals of $B_2(A_{24})_2$ and $B_3(A_{24})_2$ not only underwent [2+2] dimerization, but also displayed photomechanical behaviour. The needle-shaped crystals of $B_2(A_{24})_2$ (ranges from 0.40 mm × 0.05 mm × 0.02 mm to 1.10 mm × 0.05 mm × 0.02 mm) released the accumulated strain generated during the photoreaction by bending after 15 min of UV irradiation (Fig. 3a(i)–(vi)),[21] a phenomenon typically observed in very fine or thin crystals. However, single crystals of $B_3(A_{24})_2$, (0.80 mm × 0.75 mm × 0.10 mm) develop significant cracks on the surface (few μm wide) (Fig. 3b(i)–(vi)) and experience a surface peeling effect (Fig. S15(i)–(iv), SI) after prolonged UV exposure. The bending and morphological changes of the crystals of $B_2(A_{24})_2$ and $B_3(A_{24})_2$ upon irradiation are well supported from the field emission scanning electron microscopy images (FESEM, Fig. S16, SI) and atomic force microscopy (AFM) images (Fig. 3e, f and Fig. S17, SI). The AFM height profile exhibits a much increased average roughness (R_a) [13.8 nm for $B_2(A_{24})_2$ and 46.8 nm for $B_3(A_{24})_2$] parameter for the dimer crystals.

Crystal softness is linked to photoresponsive mechanical behaviour. Stiffness (Young's modulus, E) and hardness (H) are quantified from nanoindentation load-depth (P–h) curves (Fig. 3c, d and Fig. S18, SI). The surface mechanical properties of $B_2(A_{24})_2$ and $B_3(A_{24})_2$ correlate well with their bulk mechanical characteristics before and after irradiation. For irradiated $B_2(A_{24})_2$, a displacement of 250 nm occurred under a modest load of 67.5 μN, whereas achieving the same displacement in the non-irradiated sample required a much greater load of 776 μN. The reduction in hardness (H: from 0.4749 ± 0.1723 GPa to 0.0959 ± 0.0858 GPa) and Young's modulus (E: from 9.50 ± 1.99 GPa to 1.55 ± 0.7305 GPa) indicates more softness following dimerization accompanied bending. The hardness (H) is comparable to those of the frequently reported organic crystals in the literature that undergo elastic or elasto-plastic bending upon photodimerization (Table S5, SI). In comparison, the $B_3(A_{24})_2$ crystals are substantially stiffer, requiring a force of 6.428 mN to achieve a 250 nm indent. After irradiation, these crystals become more fragile, with only 4.834 mN needed for the same displacement. The corresponding drop in hardness (H: from 4.18 ± 1.06 GPa to 4.09 ± 0.3039 GPa) and modulus (E: from 56.83 ± 2.96 GPa to 55.25 ± 3.09 GPa) further reflects the decline in mechanical robustness post-irradiation.

Although the crystals were intact after photoirradiation, they were found to be opaque and non-diffracting by single-crystal X-ray diffraction. The PXRD patterns of the irradiated material were found to be significantly altered from the parent crystals (Fig. S2, SI). Good quality single crystals of ethylene diamine salts of HH-*rctt*-cpcb dimers namely *d*-$B_2(A_{24})_2$ and *d*-$B_2(A_{34})_2$ were recrystallised from a DMSO-acetone (1 : 3, v/v) and MeOH-nitrobenzene (3 : 0.5, v/v) mixture, respectively. Crystal structure analysis shows the formation of a head-to-head dimer in both cases, as evident in the ^{1}H NMR spectra (Fig. 4). The crystals structures of both were found to be isostructural and crystallise in the $P2_1/c$ space group. The asymmetric units contain one full

Table 2 Photodimerization yields (%) after 24 hours of the crystals, as-synthesised materials and organogels of all the salts

	% Yield		
Salts	As-synthesised	Crystals	Gels
$B_2(A_{24})_2$	~90	~90	~29
$B_2(A_{34})_2$	~85	—	~72
$B_3(A_{24})_2$	100	100	~58
$B_3(A_{34})_2$	~85	—	~40

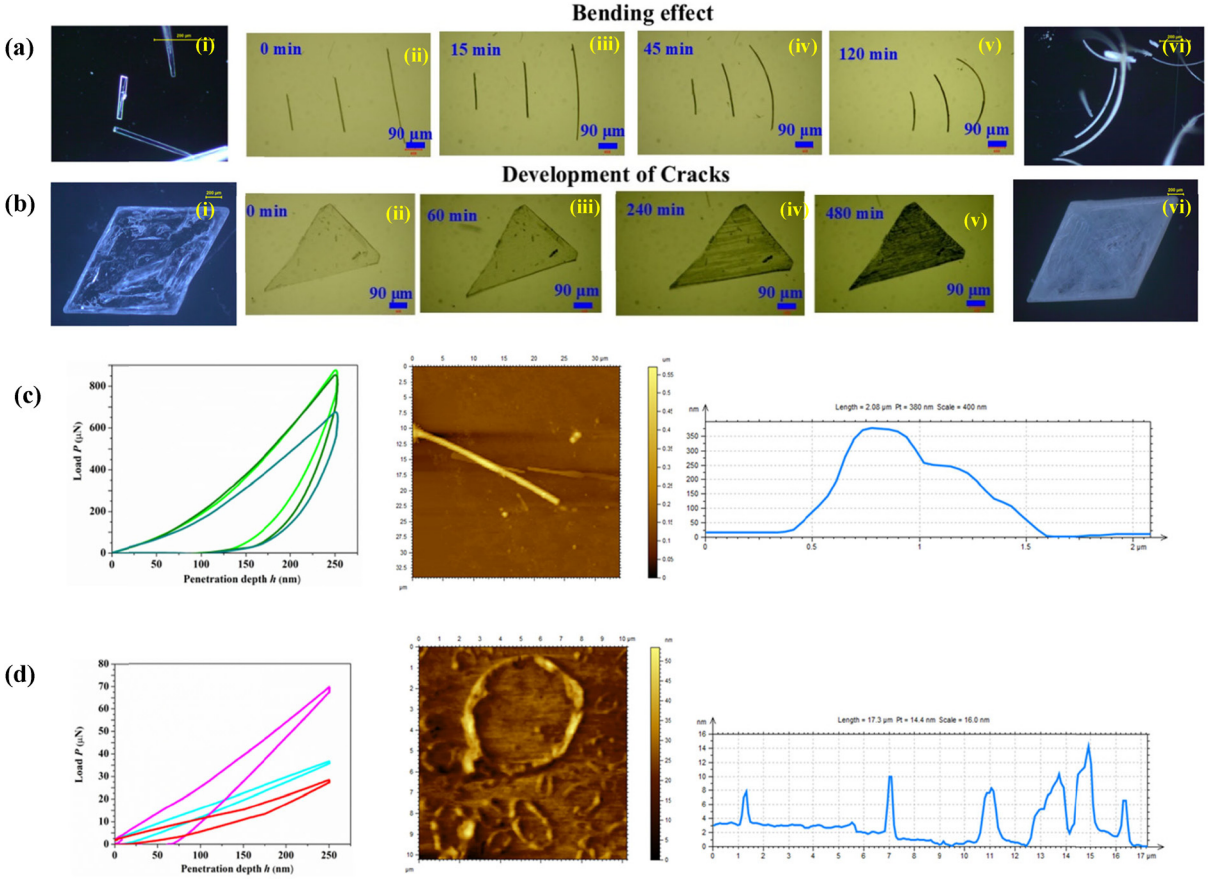

Fig. 3 Optical microscope images illustrating bending (a(i)–(vi)) in single crystals of $B_2(A_{24})_2$ and (b(i)–(vi)) the development of cracks in the $B_3(A_{24})_2$crystals; (i) and (vi) are dark field images before and after the irradiation in both cases. *P–h* curve for $B_2(A_{24})_2$ (c) before and (d) after irradiation. AFM images for $B_2(A_{24})_2$ (e) before and (f) after irradiation; from left to right: 2D AFM and 3D AFM height profile.

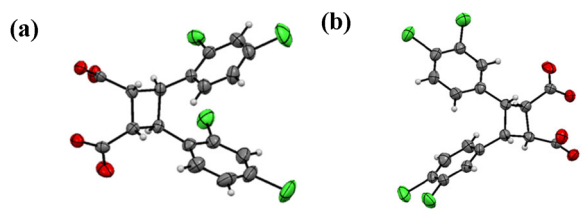

Fig. 4 ORTEP drawing of the head-to-head dimer of (a) $B_2(A_{24})_2$, and (b) $B_2(A_{34})_2$.

unit of ethylenediamine cation with the HH-*rctt*-2,4/3,4-cpcb dimer. Two carboxylates of HH-*rctt*-2,4/3,4-cpcb dimer form seven N–H···O hydrogen bonds with the ethylenediammonium cation (N···O: 2.745(4) Å–3.300(4) Å; <N–H···O: 112°–174°). Such type of hydrogen-bonding packs to form a bilayer structure of alternating hydrophilic and hydrophobic layers, similar to the $B_2(A_{24})_2$ monomer (Fig. S19, SI). The C–C bond length of 1.582 Å (in case of $B_2(A_{24})_2$) and 1.575 Å $B_2(A_{34})_2$ confirms the formation of cyclobutane rings. Moreover, solid state photoluminescence (PL) spectra of the salts after photoirradiation showed greatly quenched luminescence emission profiles from before, mainly due to the loss of conjugation on dimerization (Fig. S20, SI).

Leveraging the abundant N^+–H···O^- hydrogen bonding interaction and high propensity of iodine to engage in intra/inter halogen bonding interaction (–Cl···I, –N···I, –O···I), we explore the ability of the salt's to absorb iodine vapour. To conduct the investigation, a vial containing 20 mg of as-synthesised salts was placed into the sealed container containing solid iodine beads. The sealed container was heated at 70 °C for 5 hours to ensure complete volatilization of iodine. To monitor the uptake kinetics, samples were removed at 1-hour intervals, allowed to cool to room temperature, and weighed. These experiments were repeated on three different batches of salt samples and it was found that the results are consistent. After adsorption of I_2 by the B_2 salts, the sample turned sticky and adhered strongly to the container, making it difficult to remove. Various analyses including visual colour changes, TGA, and X-ray photoelectron spectroscopy confirmed effective iodine uptake by the B_3 and B_4 salts (Fig. 5a and Fig. S21, S22, SI). The highest amount of iodine loading was found to be 330 mg g^{-1} for the $B_3(A_{24})_2$ salt (Fig. 5b). $I_2@B_3(A_{24})_2$ and $I_2@B_4(A_{34})_2$ contain ~0.7 and ~0.2 molecules of I_2 per salt molecule, respectively, whereas $I_2@B_4(A_{24})_2$ and $I_2@B_4(A_{34})_2$ absorb ~0.3 and ~0.1 molecules of I_2 per salt molecule, respectively. The I_2 uptake values are comparable to the frequently reported

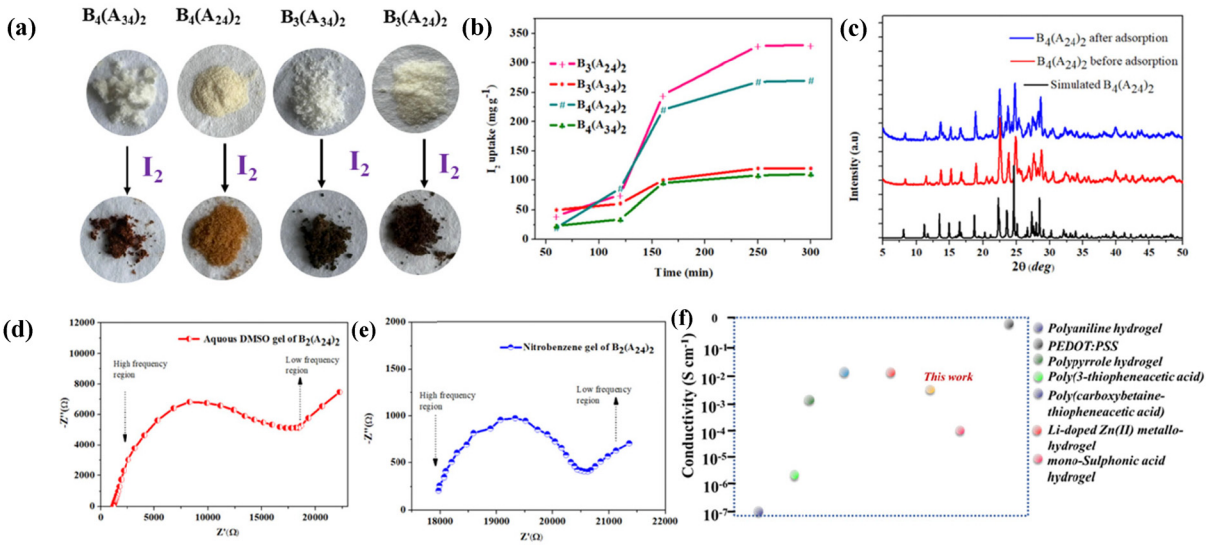

Fig. 5 (a) Photographs of the salts before and after exposure to iodine; (b) iodine uptake in B_3 and B_4 salts as a function of time. Note that the $B_3(A_{34})_2$ and $B_4(A_{34})_2$ plots overlay almost exactly. (d) PXRD data showing no change after iodine adsorption in $B_4(A_{24})_2$; a similar observation was shown for all the other cases (Fig. S25, SI); Nyquist impedance plots of the (e) aqueous-DMSO gel and (f) nitrobenzene gel of $B_2(A_{24})_2$. (g) Comparison of conductivity of different hydrogels.

adsorption values of porous organic polymers (POPs) and MOFs (Table S6). TGA revealed that pristine $B_3(A_{24})_2$ is stable up to ≈365 °C, whereas I_2 absorbed materials ($I_2@B_3(A_{24})_2$) are stable up to ≈330 °C. The TGA of $I_2@B_3(A_{24})_2$ displayed an initial weight loss of 14.07% at ≈157 °C, corresponding to the adsorbed iodine. Similarly, the TGA of $B_4(A_{24})_2$ and $I_2@B_4(A_{24})_2$ indicates that they are stable up to ≈335 °C and ≈238 °C, respectively. $I_2@B_4(A_{24})_2$ undergoes 12% weight loss at ≈125 °C due to the release of adsorbed iodine (Fig. S21, SI).

The FESEM images of $I_2@B_3(A_{24})_2$ revealed no significant change in surface morphology except for iodine crystals adhered to the surface (Fig. S23, SI). The elemental mapping and energy dispersive X-ray spectroscopy (EDX) analysis confirmed the homogenous distribution of iodine along with the C, N, O and Cl within the $I_2@B_3(A_{24})_2$ (Fig. S23, SI). The FT-IR spectrum of the salts before and after I_2 adsorption were compared; the spectra were nearly superimposable (Fig. S24, SI), suggesting weak interactions of I_2 with salts.

The PXRD patterns of the as-synthesized salts before and after I_2 adsorption were in good agreement, indicating no phase change due to I_2 adsorption, which further supported physical adsorption of I_2 through weak interactions (Fig. 5c and Fig. S25, SI). Raman spectra revealed consistent peaks around 109 cm^{-1} in all I_2 adsorbed B_3 and B_4 salts, due to symmetric stretching of perturbed I_3^- ions, and the symmetric stretching of perturbed I_2 appears around 168 cm^{-1} (Fig. S26, SI).

Previous studies on carboxylate salts have demonstrated high electrical conductivity owing to N^+–H···O^- hydrogen bonding interaction.[40] Encouraged by this and by the presence immobilized solvents (DMSO, H_2O) within the gel matrix, we performed electrochemical impedance spectroscopy (EIS) measurements to explore the conductance properties of the organogel. The development of highly electrically conductive materials is essential for advancing next-generation technologies, such as electrochemical sensing, fuel cells, and flexible electronic devices.[54] Aqueous-DMSO gels are advanced conductive materials designed particularly for applications requiring high electrical conductivity and anti-freezing properties.[55] The fact that the OGs were able to light an LED bulb when connected through copper electrodes in a home-made electrical circuit powered by a battery confirmed their ability to conduct electricity (Fig. S27, SI). Nyquist plots show a semicircle in the high frequency region followed by a linear evolution in the low frequency region. The conductivity value was calculated to be 5.2 × 10^{-3} S cm^{-1} and 3.4 × 10^{-4} S cm^{-1} at 25 °C from the equation $\sigma = d/(R_b \times A)$, where R_b, d and A are the bulk resistance, thickness and area for the $B_2(A_{24})_2$ aqueous-DMSO and nitrobenzene gel, respectively (Fig. 5d, e and Fig. S28a, SI). Electrical conductivity cannot be measured effectively with pure water-DMSO solution because of the absence of sufficient free, mobile ions. According to the current literature, the conductivity values are comparable with those of a few polymeric and metallo-supramolecular hydrogels (Fig. 5f and ref. S6–S11). It may be noted that during the measurements, no degradation of the hydrogel was observed. Measuring the conductivity of the xerogels in the pelleted structure proved ineffective as they are essentially non-conducting at 100 μA current flow because dehydration eliminates their primary charge carriers.[56] The conductivities of the iodine-loaded xerogel pellets at 25 °C are calculated to be in the range of 10^{-5}–10^{-6} S cm^{-1}(Fig. S28b and c).

Conclusions

In conclusion, we have successfully developed a series of new organic materials; alkyl diamine (B_{2-4}) salts of 2,4/3,4- dichloro cinnamic acid (A_{24} or A_{34}). By leveraging the chloro-substitution

strategy to direct β-type packing, we have demonstrated efficient [2+2] photodimerization in single crystals, as-synthesized materials and organogels. The crystals of $B_2(A_{24})_2$ and $B_3(A_{24})_2$ showed striking [2+2] dimerization mediated photomechanical responses, including bending, development of cracks and surface peeling. Nanoindentation and AFM analyses quantified this behavior, revealing a significant reduction in Young's modulus and hardness after irradiation, consistent with macroscopic crystal ''softening.'' Four of the six salt combinations formed stable, thermo-reversible organogels. These gels showed [2+2] photoreactivity comparable to their crystalline or as-synthesised counterparts, representing the first examples of their kind. The B_3 and B_4 salts exhibited reasonable iodine capture capacity (up to 330 mg g^{-1}), owing to weak interactions with the –Cl functionality. These materials can be potential platforms for iodine remediation. Furthermore, the organogels showed good electrical conductivity (5.2×10^{-3} S cm^{-1}) at room temperature. This positions these 'salt-gels' as promising candidates for flexible electronics and conductive sensors.

Author contributions

All authors have given approval to the final version of the manuscript.

Conflicts of interest

There are no conflicts to declare.

Data availability

The supporting information of this study's findings are included in the article and supplementary information (SI). The supporting information of this article's study including Experimental Details/Methods, FT-IR spectra, Crystallographic parameters, Rheological characterisation, FESEM images, PXRD analysis, ^{1}H-NMR spectra, MALDI-ToF analysis, AFM analysis, *P–h* curve, PL spectra, XPS spectra, EDS analysis, Raman spectra, Comparison table, EIS plots are included in the Supplementary Information (SI). See DOI: https://doi.org/10.1039/d6ma00366d.

CCDC 2533551–2533556 contain the supplementary crystallographic data for this paper.[57a–f]

Acknowledgements

We acknowledge the financial support from DST-SERB (CRG/2022/000606), New Delhi, India. S. S. and D. P. thank IIT Kharagpur for their research fellowships.

References

1 O. S. Bushuyev, T. C. Corkery, C. J. Barrett and T. Friščić, Photo-mechanical azobenzene cocrystals and in situ X-ray diffraction monitoring of their optically-induced crystal-to-crystal isomerisation, *Chem. Sci.*, 2014, **5**, 3158–3164.
2 T. Muraoka, K. Kinbara and T. Aida, Mechanical twisting of a guest by a photoresponsive host, *Nature*, 2006, **440**, 512–515.
3 K. G. Yager and C. J. Barrett, Novel photo-switching using azobenzene functional materials, *J. Photochem. Photobiol., A*, 2006, **182**, 250–261.
4 J. Hu, X. Li, Y. Ni, S. Ma and H. Yu, A Programmable and Biomimetic Photo-Actuator: A Composite of a Photo-Liquefiable Azo-benzene Derivative and Commercial Plastic Film, *J. Mater. Chem. C*, 2018, **6**, 10815–10821.
5 S. Mondal, P. Tanari, S. Roy, S. Bhunia, R. Chowdhury, A. K. Pal, A. Datta, B. Pal and C. M. Reddy, Autonomous self-healing organic crystals for nonlinear optics, *Nat. Commun.*, 2023, **14**, 6589.
6 E. Hatano, M. Morimoto, T. Imai, K. Hyodo, A. Fujimoto, R. Nishimura, A. Sekine, N. Yasuda, S. Yokojima and S. Nakamura, Photosalient Phenomena that Mimic Impatiens Are Observed in Hollow Crystals of Diarylethene with a Perfluorocyclohexene Ring, *Angew. Chem., Int. Ed.*, 2017, **56**, 12576–12580.
7 L. Zhu, F. Tong, C. Salinas, M. K. Al-Muhanna, F. S. Tham, D. Kisailus, R. O. Al-Kaysi and C. J. Bardeen, Improved Solid-State Photomechanical Materials by Fluorine Substitution of 9-Anthracene Carboxylic Acid, *Chem. Mater.*, 2014, **26**, 6007–6015.
8 P. Naumov, S. C. Sahoo, B. A. Zakharov and E. V. Boldyreva, Dynamic single crystals: kinematic analysis of photoinduced crystal jumping (the photosalient effect), *Angew. Chem., Int. Ed.*, 2013, **52**, 9990–9995.
9 R. Medishetty, S. C. Sahoo, C. E. Mulijanto, P. Naumov and J. J. Vittal, Photosalient Behavior of Photoreactive Crystals, *Chem. Mater.*, 2015, **27**, 1821–1829.
10 H. R. Wang, P. Chen, Z. Wu, J. Y. Zhao, J. B. Sun and R. Lu, Bending, curling, rolling and salient behaviors of molecular crystals driven by [2+2] cycloaddition of styrylbenzoxazole derivative, *Angew. Chem., Int. Ed.*, 2017, **56**, 9463–9467.
11 V. Gude, P. S. Choubey, S. Das, B. N. S. Bhaktha, C. M. Reddy and K. Biradha, Elastic Orange Emissive Single Crystals of 1,3-Diamino-2,4,5,6-Tetrabromobenzene as Flexible Optical Waveguides, *J. Mater. Chem. C*, 2021, **9**, 9465–9472.
12 B. B. Rath and J. J. Vittal, Photoreactive Crystals Exhibiting [2+2] Photocycloaddition Reaction and Dynamic Effects, *Acc. Chem. Res.*, 2022, **55**, 1445–1455.
13 K. Yuhara and K. Tanaka, The Photosalient Effect and Thermochromic Luminescence Based on o-Carborane-Assisted π-Stacking in the Crystalline State, *Angew. Chem., Int. Ed.*, 2024, **63**, e202319712.
14 T. Nishiuchi, K. Kisaka and T. Kubo, Synthesis of Anthracene-Based Cyclic π-Clusters and Elucidation of their Properties Originating from Congested Aromatic Planes, *Angew. Chem., Int. Ed.*, 2021, **60**, 5400–5406.
15 K. Kato, T. Seki and H. Ito, 9-Isocyanoanthracene)gold(I) Complexes Exhibiting Two Modes of Crystal Jumps by Different Structure Change Mechanisms, *Inorg. Chem.*, 2021, **60**, 10849–10856.

16 E. Ahmed, D. P. Karothu and P. Naumov, Crystal Adaptronics: Mechanically Reconfigurable Elastic and Superelastic Molecular Crystals, *Angew. Chem., Int. Ed.*, 2018, **57**, 8837–8846.

17 Q. Zhang, Y. Wang, X.-Y. Huang, Q. Liu, P. Braunstein and J.-P. Lang, Wavelength-Controlled Stepwise Photocycloaddition Reactions and Photomechanical Motions of a Cd(II) Complex, *CCS Chem.*, 2026, **8**, 261–270.

18 Y. Wang, Q. Zhang, X.-Y. Huang, Q. Liu and J.-P. Lang, Modulating Solid-State Photocycloaddition Kinetics via Ligand Substituents and Crystal Structures in One-Dimensional Coordination Polymers, *J. Am. Chem. Soc.*, 2025, **147**, 22192–22200.

19 G. K. Kole, L. L. Koh, S. Y. Lee, S. S. Lee and J. J. Vittal, A new ligand for metal–organic framework and co-crystal synthesis: mechanochemical route to *rctt*-1,2,3,4-tetrakis-(4′-carboxyphenyl)-cyclobutane, *Chem. Commun.*, 2010, **46**, 3660–3662.

20 Y. Wang, Q. Zhang, Q. Liu, B. F. Abrahams and J.-P. Lang, The Use of Photocycloaddition Reactions to Drive Mechanical Motions Resembling Humanoid Movements, *Angew. Chem., Int. Ed.*, 2024, **63**, e202409472.

21 B. B. Rath and J. J. Vittal, Single-crystal-to-single-crystal [2+2] photocycloaddition reaction in a photosalient one-Dimensional coordination polymer of Pb(II), *J. Am. Chem. Soc.*, 2020, **142**, 20117–20123.

22 S. Kusumoto, K. Sato, K. Muraie, S. Masuda, K. Rakumitsu, Y. Kim and Y. Koide, Photosalient ionic cocrystal composed of trimesic acid and 4-styrylpyridine, *CrystEngComm*, 2023, **25**, 909–912.

23 R. Medishetty, A. Husain, Z. Z. Bai, T. Runčevski, R. E. Dinnebier, P. Naumov and J. J. Vittal, Single crystals popping under UV light: a photosalient effect triggered by a [2+2] cycloaddition reaction, *Angew. Chem., Int. Ed.*, 2014, **53**, 5907–5911.

24 R. O. Al-Kaysi, A. M. Müller and C. J. Bardeen, Photochemically Driven Shape Changes of Crystalline Organic Nanorods, *J. Am. Chem. Soc.*, 2006, **128**, 15938–15939.

25 R. Mandal, A. Garai, S. Peli, P. K. Datta and K. Biradha, Photoinduced Bending of Single Crystals of a Linear Bis-Olefin *via* Water-templated Solid-State [2+2] Photopolymerization Reaction, *Chem. – Eur. J.*, 2020, **26**, 396–400.

26 J.-A. Lv, Y. Liu, J. Wei, E. Chen, L. Qin and Y. Yu, Photocontrol of fluid slugs in liquid crystal polymer microactuators, *Nature*, 2016, **537**, 179–184.

27 C. Li, A. Iscen, L. C. Palmer, G. C. Schatz and S. I. Stupp, Light-Driven Expansion of Spiropyran Hydrogels, *J. Am. Chem. Soc.*, 2020, **142**, 8447–8453.

28 H. Yu and T. Ikeda, Photocontrollable Liquid-Crystalline Actuators, *Adv. Mater.*, 2011, **23**, 2149–2180.

29 K. Biradha and R. Santra, Crystal Engineering of Topochemical Solid State Reactions, *Chem. Soc. Rev.*, 2013, **42**, 950–967.

30 S. Roy and K. Biradha, Two-Component Supramolecular Organic Hosts as Colorimetric Indicators for Aromatic Guests: Visual Molecular Recognition *via* Cation−π Interactions, *Cryst. Growth Des.*, 2011, **11**, 4120–4128.

31 A. Garai and K. Biradha, Binary and Ternary Salts and Cocrystals of 2-(2-(Pyridine-4-yl)vinyl)-1*H*-benzimidazole with Aromatic Carboxylic Acids: Solid-State [2+2] Reactions, Photoluminescence, and Ammonia-Sensing Properties, *Cryst. Growth Des.*, 2019, **19**, 4602–4612.

32 G. K. Kole, G. K. Tan and J. J. Vittal, Crystal engineering studies on the salts of *trans*-4,4′-stilbenedicarboxylic acid in the context of solid state [2+2] cycloaddition reaction, *CrystEngComm*, 2011, **13**, 3138–3145.

33 A. Matsumoto, K. Sada, K. Tashiro, M. Miyata, T. Tsubouchi, T. Tanaka, T. Odani, S. Nagahama, T. Tanaka, K. Inoue, S. Saragai and S. Nakamoto, Reaction Principles and Crystal Structure Design for the Topochemical Polymerization of 1,3-Dienes, *Angew. Chem., Int. Ed.*, 2002, **41**, 2502–2505.

34 M. Ayabe, T. Kishida, N. Fujita, K. Sada and S. Shinkai, Binary Organogelators Which Show Light and Temperature Responsiveness, *Org. Biomol. Chem.*, 2003, **1**, 2744–2747.

35 A. Natarajan, J. T. Mague, K. Venkatesan and R. Ramamurthy, Large Molecular Motions Are Tolerated in Crystals of Diamine Double Salt of *trans*-Chlorocinnamic Acids with *trans*-1,2-Diaminocyclohexane, *Org. Lett.*, 2005, **7**, 1895–1898.

36 Y. Ito, B. Borecka, J. Trotter and J. R. Scheffer, Control of solid-state photodimerization of trans-cinnamic acid by double salt formation with diamines, *Tetrahedron Lett.*, 1995, **36**, 6083–6086.

37 Y. Ito, B. Borecka, G. Olovsson, J. Trotter and J. R. Scheffer, Control of the Solid-state photodimerization of some derivatives and analogs of trans-cinnamic acid by ethylenediamine, *Tetrahedron Lett.*, 1995, **36**, 6087–6090.

38 Y. Xie, X. Ding, J. Wang and G. Ye, Hydrogen-bonding assembly meets anion coordination chemistry: framework shaping and polarity tuning for xenon/krypton separation, *Angew. Chem., Int. Ed.*, 2023, **62**, e202313951.

39 L. Feng, Y. Yuan, B. Yan, T. Feng, Y. Jian, J. Zhang, W. Sun, K. Lin, G. Luo and N. Wang, Halogen hydrogen-bonded organic framework (XHOF) constructed by singlet open-shell diradical for efficient photoreduction of U(VI), *Nat. Commun.*, 2022, **13**, 1389.

40 S. Roy, S. P. Mondal, S. K. Ray and K. Biradha, A Photoswitchable and Photoluminescent Organic Semiconductor Based on Cation-π and Carboxylate-Pyridinium Interactions: A Supramolecular Approach, *Angew. Chem., Int. Ed.*, 2012, **51**, 12012–12015.

41 G. Mahata, S. Roy and K. Biradha, Separation of Isomers of Sulfophthalic Acid by Guest Induced Host Framework Formation with 4,4′-Bipyridine, *Chem. Commun.*, 2011, **47**, 6614–6616.

42 M. O'Shaughnessy, J. Glover, R. Hafizi, M. Barhi, R. Clowes, S. Y. Chong, S. P. Argent, G. M. Day and A. I. Cooper, Porous isoreticular non-metal organic frameworks, *Nature*, 2024, **630**, 102–108.

43 A. Ballabh, D. R. Trivedi and P. Dastidar, New Series of Organogelators Derived from a Combinatorial Library of Primary Ammonium Monocarboxylate Salts, *Chem. Mater.*, 2006, **18**, 3795–3800.

44 U. K. Das, D. R. Trivedi, N. N. Adarsh and P. Dastidar, Supramolecular Synthons in Noncovalent Synthesis of a Class of Gelators Derived from Simple Organic Salts: Instant Gelation of Organic Fluids at Room Temperature via in Situ Synthesis of the Gelators, *J. Org. Chem.*, 2009, **74**, 7111–7121.
45 A. Dey and K. Biradha, Photochemical Reactions in Supramolecular Assemblies of Gels: Dimerizations and Polymerizations via Pericyclic Reactions, *Isr. J. Chem.*, 2018, **58**, 1–14.
46 S. Samai, P. Ghosh and K. Biradha, Does Crystal or Gel Matter to Stereochemistry of a Reaction? Silver Complexation-Promoted Solid-State [2+2] Reaction of an Unsymmetrical Olefin, *Chem. Commun.*, 2013, **49**, 4181–4183.
47 S. Bedi and K. Biradha, [2+2] Dimerization of a V-Shaped Diene in Organogel, Xerogel, and Single Crystals: Structural Insights into the Self-Assembly of Gelator Molecules in Organogels and Xerogels, *Cryst. Growth Des.*, 2025, **25**, 5532–5542.
48 S. Sultana, R. Mandal and K. Biradha, Photo Responsive Metal-Organic Gels of Rigid Phenylene-1,3-di-Substituted Angular Diene with Metal Halides: Gel-to-Gel Transformation triggered by [2+2] Polymerization, *Dalton Trans.*, 2024, **53**, 4797–4804.
49 M. D. Dawn, S. Patra, D. Banerjee and K. Biradha, Switching of light responsive metal–organic gels from insulator to semiconductor: flexible smart semiconducting membranes for optoelectronic device fabrication, *J. Mater. Chem. C*, 2025, **13**, 15862–15872.
50 G. M. J. Schmidt, Photodimerization in the Solid State, *Pure Appl. Chem.*, 1971, **27**, 647–678.
51 S. Naskar, R. Moi, I. Das and K. Biradha, Halogen···Halogen and Halogen···π Interactions Enabled Reversible Photo-Oligomerization of Conjugated Dienones: Visible Light Triggered Single-Crystal-to-Single-Crystal Transformation, *Angew. Chem., Int. Ed.*, 2022, **61**, e202204141.
52 J. A. R. P. Sarma and G. R. Desiraju, The role of Cl···Cl and C–H···O interactions in the crystal engineering of 4-Å. short-axis structures, *Acc. Chem. Res.*, 1986, **19**, 222–228.
53 D. Pal, S. Saha and K. Biradha, N–H···N Hydrogen-Bonded Helices to Halogen···Halogen and Cation···π Interactions in Aprotic, Monoprotic, and Biprotic Halogen-Substituted Lophines, *Cryst. Growth Des.*, 2025, **25**, 1880–1891.
54 K. Biradha, M. D. Dawn, S. Sultana and P. Paul, Stimuli-Responsive Transformations in Metal-Organic Gels: Mechanistic Insights, Characterization, and Functional Applications, *Coord. Chem. Rev.*, 2026, **552**, 217513.
55 Q. Rong, W. Lei, L. Chen, Y. Yin, J. Zhou and M. Liu, Anti-Freezing, Conductive Self-Healing Organohydrogels with Stable Strain-Sensitivity at Subzero Temperatures, *Angew. Chem., Int. Ed.*, 2017, **56**, 14159–14163.
56 C. M. Julien and A. Mauger, Fabrication of $Li_4Ti_5O_{12}$ (LTO) as Anode Material for Li-Ion Batteries, *Micromachines*, 2024, **15**, 310.
57 (*a*) CCDC 2533551: Experimental Crystal Structure Determination, 2026, DOI: 10.5517/ccdc.csd.cc2r1cgn; (*b*) CCDC 2533552: Experimental Crystal Structure Determination, 2026, DOI: 10.5517/ccdc.csd.cc2r1chp; (*c*) CCDC 2533553: Experimental Crystal Structure Determination, 2026, DOI: 10.5517/ccdc.csd.cc2r1cjq; (*d*) CCDC 2533554: Experimental Crystal Structure Determination, 2026, DOI: 10.5517/ccdc.csd.cc2r1ckr; (*e*) CCDC 2533555: Experimental Crystal Structure Determination, 2026, DOI: 10.5517/ccdc.csd.cc2r1cls; (*f*) CCDC 2533556: Experimental Crystal Structure Determination, 2026, DOI: 10.5517/ccdc.csd.cc2r1cmt.